



Universiteit
Leiden
The Netherlands

Quantum and electrochemical interplays in hydrogenated graphene

Jiang, L.; Fu, W.; Birdja, Y.Y.; Koper, M.T.M.; Schneider, G.F.

Citation

Jiang, L., Fu, W., Birdja, Y. Y., Koper, M. T. M., & Schneider, G. F. (2018). Quantum and electrochemical interplays in hydrogenated graphene. *Nature Communications*, 9, 793. doi:10.1038/s41467-018-03026-0

Version: Not Applicable (or Unknown)

License: [Leiden University Non-exclusive license](#)

Downloaded from: <https://hdl.handle.net/1887/61388>


Note: To cite this publication please use the final published version (if applicable).

ARTICLE

DOI: 10.1038/s41467-018-03026-0

OPEN

Quantum and electrochemical interplays in hydrogenated graphene

Lin Jiang¹, Wangyang Fu ¹, Yuvraj Y. Birdja¹, Marc T.M. Koper¹ & Grégory F. Schneider¹

The design of electrochemically gated graphene field-effect transistors for detecting charged species in real time, greatly depends on our ability to understand and maintain a low level of electrochemical current. Here, we exploit the interplay between the electrical in-plane transport and the electrochemical activity of graphene. We found that the addition of one H- sp^3 defect per hundred thousand carbon atoms reduces the electron transfer rate of the graphene basal plane by more than five times while preserving its excellent carrier mobility. Remarkably, the quantum capacitance provides insight into the changes of the electronic structure of graphene upon hydrogenation, which predicts well the suppression of the electrochemical activity based on the non-adiabatic theory of electron transfer. Thus, our work unravels the interplay between the quantum transport and electrochemical kinetics of graphene and suggests hydrogenated graphene as a potent material for sensing applications with performances going beyond previously reported graphene transistor-based sensors.

¹Leiden University, Faculty of Science, Leiden Institute of Chemistry, Einsteinweg 55, Leiden, 2333CC, The Netherlands. Lin Jiang and Wangyang Fu contributed equally to this work. Correspondence and requests for materials should be addressed to G.F.S. (email: g.f.schneider@chem.leidenuniv.nl)

Graphene is unique among other solid-state materials in that all carbon atoms are located on the surface, making the graphene surface highly sensitive for the detection of changes in the environment. Particularly, the concept of electrochemically gated graphene field-effect transistor (GFET) enables the label-free detection of charged molecules on a small footprint upon their bindings at/near the graphene surface:^{1,2} a binding event modulates the electrical current in the graphene channel through the local variation of the electric field^{3,4}. The creation of practical electrochemically gated GFETs for detecting charged species, however, greatly depends on our ability to understand and maintain a low level of electrochemical current. Specifically, the electrochemical current roots on the current flowing between the graphene channel and redox active molecules in the solution phase.

Complementary to GFET sensors, the electrochemical current towards a redox probe in solution has been widely studied and is at the basis of graphene electrochemical (GEC) sensors. Previous studies have revealed that the electrochemical activity is largely sensitive to the intrinsic chemical structure of the graphene basal plane^{5–8}. Among the multiple approaches used to chemically modify graphene, for example, post-growth chemical modifications using various oxidative reactions^{9–11} are effective routes to incorporate oxygen atoms, although at the cost of a poor control over the resulting functional groups (i.e., epoxy, carbonyl, carboxylic acid, alcohol, all at the same time). Particularly, hydrogenated or fluorinated graphene endows a large range of possibilities to progressively tweak graphene with sp^3 defects without significantly pinning the lattice integrity or breaking the resilient basal plane C–C bonds^{12–15}.

Here, a low density of H- sp^3 defects are introduced into monolayer graphene using a hydrogen plasma. We found that only 1 s of plasma treatment is able to render a pristine graphene surface (with few H- sp^3 defects) from the as-grown graphene (referred as untreated graphene) by removing the adsorbed hydrocarbons at the surface, as manifested by the dramatic boost in the electron transfer rate. Importantly, further addition of only one H- sp^3 defect per hundred thousand carbon atoms (more than 1 s of hydrogen plasma), allows us to substantially reduce the electron transfer rate of hydrogenated graphene (H-graphene)

compared to pristine graphene. Remarkably, we successfully correlated the degradation of the electrochemical kinetics of the graphene basal plane with the density of states (DOS) by tuning the density of H- sp^3 defects. Although the H- sp^3 termination could contribute to a higher electrochemical activity, the electronic structure (DOS) in graphene plays an even more decisive role in the rate of electron transfer between graphene and redox probes for a low defect density, indicating a non-adiabatic transfer process on the graphene basal plane.

Results

Raman characterization. To determine the density and the nature of the defects induced by hydrogen radicals, we conducted Raman spectroscopy (Fig. 1a) and mapping (Supplementary Figure 1a) on graphene prepared by chemical vapor deposition (CVD). The similarities between the Raman spectra for both CVD and exfoliated graphene (Supplementary Figure 2) indicate that the defects induced by the H₂ plasma—particularly the defect density n_D —are respectively equivalent. Importantly, the D peak at ~ 1340 cm⁻¹, due to single phonon intervalley scattering events, is caused by the apparition of H- sp^3 defects¹⁶. After a hydrogenation time of 10 s, a D' peak at 1620 cm⁻¹ appears in the Raman spectrum as a shoulder of the G peak. The D' peak also associates with H- sp^3 defects¹⁷. The values determined for $I(D)/I(D')$ (~ 10) after 30 s and 60 s of hydrogenation are consistent with a previous report and confirm the sp^3 nature of hydrogenated defects (Fig. 1b)¹⁸. Meanwhile, the intensity ratio $I(2D)/I(G)$, a sensitive parameter to graphene doping, decreases continuously from 2.2 to 1.3 upon extended hydrogenation (Fig. 1c)^{19,20}.

Derived from the $I(D)/I(G)$ ratio (a quantitative indicator of point defects in graphene samples)²¹, the defect density n_D increases linearly with the hydrogenation time from $n_D = (0.2 \pm 0.3) \times 10^{10}$ cm⁻² at 0 s (untreated graphene) to $n_D = (3.2 \pm 0.7) \times 10^{11}$ cm⁻² at 60 s, corresponding to a decrease in the average distance between defect sites (L_D) from 122.6 nm to 10.0 nm (Fig. 1d, see Supplementary Note 1 for the calculation of n_D and L_D). Notably, the Raman mapping (D peak intensity) in Supplementary Figure 1b on exfoliated graphene flakes (which

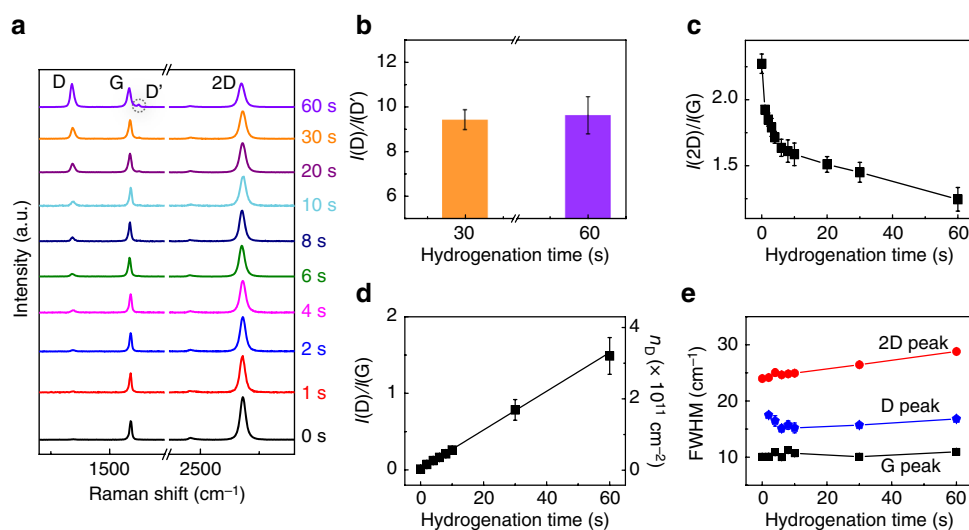


Fig. 1 Raman characterization of hydrogenated graphene. **a** Averaged Raman spectra of CVD graphene on a Si/SiO₂ substrate after 0–60 s of H₂ plasma (10 W, 1.0 mbar). **b** The intensity ratio $I(D)/I(D')$ after 30 s and 60 s of hydrogenation. **c** The intensity ratio $I(2D)/I(G)$ for hydrogenation times ranging from 0 to 60 s. **d** The intensity ratio $I(D)/I(G)$ and the derived defect density n_D , plotted vs the hydrogenation time. The error bars include results from both exfoliated and CVD graphene. **e** The FWHM of the 2D, G, and D peaks vs the hydrogenation time. The spectra are recorded using a 2.33 eV (532 nm) laser excitation. The error bars in **b–e** are the standard deviation of experimental values

contains minimal native defects, except for edges), confirms the uniform defect distribution upon hydrogenation. Other surface characterizations including scanning electron microscopy (SEM) and atomic force microscopy (AFM) (Supplementary Figure 3) further revealed the non-cracked and preserved lattice of H-graphene. Moreover, the low defect densities are also in agreement with the relatively small variations observed for the full-width at half-maximum (FWHM) of the D and G peaks ($2\text{--}5\text{ cm}^{-1}$, Fig. 1e)²². In addition, the peak broadening as hydrogenation proceeds is mainly due to the shortened lifetime of phonons caused by increasing amounts of defects^{21,22}.

Electrical transport measurement. For the device fabrication, we used high-quality, large-area CVD graphene following a facile and clean fabrication strategy as illustrated in Fig. 2a (see also Methods for details)²³. Specifically, the topside of CVD graphene (on the copper foil) was first glued on the supporting glass substrate and protected by the photopolymer of pentaerythritol tetra (3-mercaptopropionate) and triallyl-1,3,5-triazine-2,4,6-trione (PETMP-TATATO)²⁴. After the removal of backside graphene (by oxygen plasma), the copper ends were protected by covering them with a film of cellulose acetate butyrate (CAB). Then the graphene surface was exposed by etching the copper in a solution of ammonium persulfate, followed by a series of hydrogen plasma treatments to introduce defects with controlled densities. During the procedure, we employed a low-temperature annealing process ($110\text{ }^\circ\text{C}$ for $\sim 1\text{--}3\text{ h}$) to ensure a good adhesion of graphene on the underlying polymeric substrate. Only the fabricated graphene devices exhibiting mobilities on the order of $1000\text{--}1500\text{ cm}^2\text{ V}^{-1}\text{ s}^{-1}$ went through a series of field-effect, quantum capacitance, and cyclic voltammetry (CV) experiments immediately after each hydrogenation treatment. To rule out any possible sample-to-

sample variations, all the aforementioned measurements were conducted on the same graphene samples.

Figure 2a depicts a GFET device with a source (S) and a drain (D) electrode bridged via a conductive graphene channel. A gate voltage (V_g) is applied to the electrolyte solution via a Ag/AgCl reference electrode, to modulate the conductivity (G) of the GFET. Specifically, when the V_g is swept from negative to positive, the Fermi level (E_F) of graphene shifts from the valence band (hole carriers) to the conduction band (electron carriers). At the so-called charge neutrality point (CNP), the concentration of hole carriers equals that of electron carriers and the conductivity of graphene reaches its minimum G_{\min} (Fig. 2b). The slopes of the sublinear $G(V_g)$ curves are the measure for the carrier mobility μ , while the observed negative voltage of the CNP for untreated graphene implies an electron (n) doping induced by the underlying photopolymer substrate.

As hydrogenation proceeds, the CNP continuously shifts to more positive voltages, a characteristic of hole (p) doping (Fig. 2c). We attributed this doping effect to water adsorption, which occurs more readily on H-graphene than on untreated graphene^{13,25}. Upon 1 s hydrogenation, graphene exhibits a slightly increased G_{\min} (Fig. 2b) and a rather stable carrier mobility μ (Fig. 2d), suggesting that the mild hydrogenation treatment barely influences—even improves—the electrical properties of graphene²⁶. As a result, we hypothesize that the H radicals after only 1 s of hydrogenation yields a cleaner graphene by effectively removing hydrocarbon adsorbates from the surface. Further hydrogenation reduces the mobility μ (and G_{\min}) of graphene down to $\sim 750\text{ cm}^2\text{ V}^{-1}\text{ s}^{-1}$ (after 2 to 5 s of hydrogenation), after which μ stabilizes at $450\text{--}660\text{ cm}^2\text{ V}^{-1}\text{ s}^{-1}$ (after 5 to 30 s of hydrogenation). As a result, the introduction of only one H- sp^3 defect per $\sim 250,000$ down to $\sim 145,000$ sp^2 hybridized carbon atoms effectively affects the mobility of charge carriers in

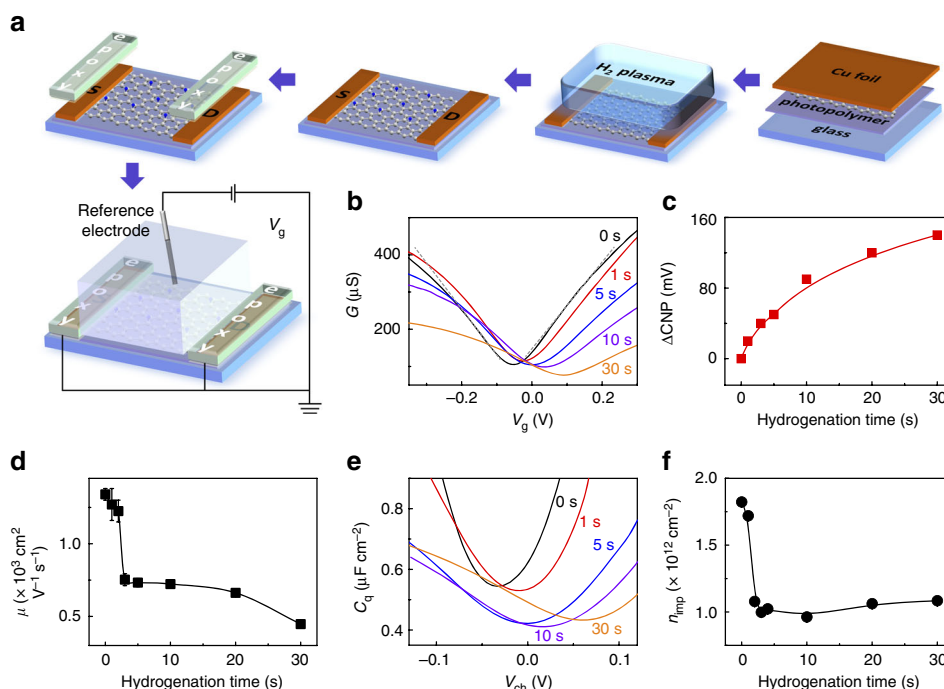


Fig. 2 Transport characteristic and quantum capacitance of CVD graphene upon hydrogenation. **a** Illustration of the field effect transistor setup fabricated from CVD graphene. **b** Room temperature conductance (G) plots as a function of the gate voltage (V_g) showing the p-doping effect upon hydrogenation from 0 to 30 s. The gray dashed line is a guide-to-the-eye, highlighting the sublinear behavior of the $G(V_g)$ curves. **c** The shifts of the charge neutrality point (CNP) upon hydrogenation. **d** The carrier mobility of graphene, μ , vs the hydrogenation time. **e** Quantum capacitance C_q of graphene measured as a function of V_{ch} for 0–30 s of hydrogenation. **f** Impurity density n_{imp} vs hydrogenation time. The electrolyte solution is 0.1 M KCl with 10 mM Tris (pH 8). The error bars in **d**, **f** are the standard deviation of experimental values

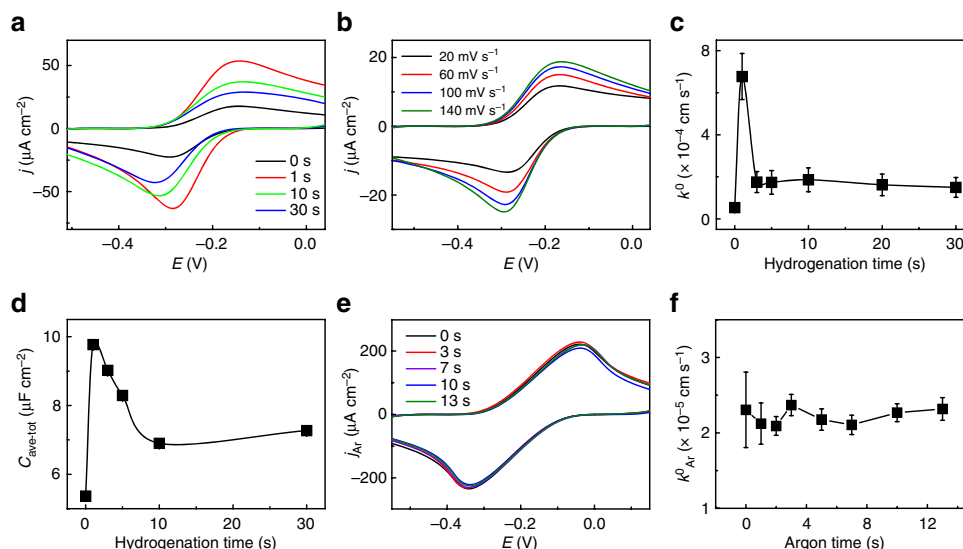


Fig. 3 Electrochemical behavior of CVD graphene upon hydrogenation. **a** Cyclic voltammograms (CVs) obtained on graphene after 0–30 s of hydrogenation at a scan rate of 100 mV s^{-1} . **b** Current density vs scan rate for untreated graphene shown in **a**. **c** The electron transfer rate k^0 vs hydrogenation time from 0 to 30 s. **d** The averaged total capacitance $C_{\text{ave-tot}}$ vs hydrogenation time from 0 to 30 s. **e** CV curves obtained on graphene after 0–13 s of Ar treatment at a scan rate of 100 mV s^{-1} . **f** k_{Ar}^0 vs argon plasma treating time from 0 to 13 s. The aqueous electrolyte solution contains 0.1 M KCl supplemented with 10 mM Tris at pH 8. The redox probe employed is 1 mM hexaammineruthenium (II)/hexaammineruthenium (III) chloride. The error bars in **c**, **d**, **f** are the standard deviation of experimental values

graphene (correspondingly $L_D = 45 \text{ nm}$ down to 35 nm). In addition to the sublinear behavior of the $G(V_g)$ curves (even after a series of hydrogenation), the remarkable decrease of G_{min} also suggests that the conductivity of hydrogenated graphene is dominated by the so-called short-range scattering mechanism^{27–29}. Such an observation is also confirmed by previous work in which hydrogenation introduced short-range scatterings in graphene lattice³⁰.

Quantum capacitance measurement. As a direct manifestation of the Pauli exclusion principle, the quantum capacitance effect in graphene is particularly prominent due to its low DOS³¹. The quantum capacitance C_q of graphene, can be directly determined as a function of the channel potential across the graphene sheet V_{ch} using an electrochemical configuration (Supplementary Figure 4)³². In Fig. 2e, the measured C_q generally displays a broad minimum, $C_{q,\text{min}}$, at the voltage of the CNP and linearly increases with V_{ch} on both sides of the CNP. Similarly to the changes in conductivity after hydrogenation (Fig. 2b), the V-shaped $C_q(V_{\text{ch}})$ curves exhibit not only positive CNP shifts, but also broader and decreased minimums with increasing hydrogenation times. In nature, $C_{q,\text{min}}$ is directly related to the density of effective charged impurities n^* (since these impurities can cause local potential fluctuations in graphene), which can reveal the global behavior of defects in graphene (Supplementary Note 2)^{19,33}. Notably, the capacitance we measured (as well as n^* values) are generally lower than those reported in previous studies. For example, untreated graphene presents a $n^* = 9.73 \times 10^{10} \text{ cm}^{-2}$, ~ 8 times lower than CVD graphene on Si/SiO₂ wafer ($n^* = 8.0 \times 10^{11} \text{ cm}^{-2}$)³². Such a remarkably lowered n^* can be ascribed to our clean fabrication strategy (Methods) which introduces less charged impurities, or reflects the differences between the substrates, which could lead to different degrees of charge transfer.

More importantly, the effective charged impurities n^* is proportional to the impurity density n_{imp} , referred as the impurities at the interfaces between graphene and the substrate, or between graphene and air, or resulting from the intrinsic defects caused by the growth or transfer of CVD graphene. In

Fig. 2f, n_{imp} decreases in the first 5 s and then settles till 30 s hydrogenation, a scenario suggesting that the mild hydrogenation (within 1–5 s) sweeps away the trapped/adsorbed charge impurities at graphene interfaces. The evolution of the defect density n_D and of the impurity density n_{imp} are closely related and critical to the electron transport and electrochemical kinetics, which we will discuss in more detail below (section Correlation of n_D with n_{imp}).

Electrochemical kinetics measurement. We employed cyclic voltammetry (CV) to investigate the electrochemical behavior of H-graphene. Specifically, we used the hexaammineruthenium (II)/hexaammineruthenium (III) redox couple (Sigma Aldrich), $\text{Ru}(\text{NH}_3)_6^{2+/3+}$, as an outer-sphere redox mediator: (i) it is surface insensitive and thus the electron transfer from the mediator to graphene (and vice versa) mainly relies on the electronic structures of the electrode and of the mediator itself and (ii) it possesses a standard potential in the vicinity of the Fermi level of graphene³⁴.

From the CVs in Fig. 3a, we determined the electrochemical activity of graphene towards the redox probe before and after 1–30 s of hydrogenation. The current densities (j) of the oxidation peak (at -170 mV) and reduction peak (at -290 mV) show that 1 s of hydrogenation is sufficient to increase the electrochemical activity of graphene by a factor of four compared to untreated graphene, while further hydrogenation brings about an immediate decrease of activity. The peak-to-peak separation (ΔE_p), a qualitative indicator of the electrochemical reversibility in graphene, displays a minimum at 1 s of hydrogenation, which is in agreement with the observed maximum for the current density (Supplementary Figure 5c).

Furthermore, from the data in Fig. 3b we extracted the heterogeneous electron transfer rate (k^0) between the graphene basal plane and the redox probe to quantitatively evaluate the electrochemical kinetics of graphene upon hydrogenation. Specifically, ΔE_p of the quasi-reversible redox peaks are below 220 mV as the scan rate (ν) increases, which meets the criteria of Nicholson's method to estimate the kinetic parameters^{34,35}

(Supplementary Note 3). Consistent with the current density depicted in Fig. 3a, the deduced values of k^0 exhibit a peaked behavior as a function of the hydrogenation time (Fig. 3c). In details, k^0 increases by up to ~ 12 fold ($6.77 \times 10^{-4} \text{ cm s}^{-1}$) after 1 s of hydrogenation compared to untreated graphene ($5.37 \times 10^{-4} \text{ cm s}^{-1}$). For longer hydrogenation times, k^0 sharply drops down to $\sim 1.70 \times 10^{-4} \text{ cm s}^{-1}$ within 5 s and stabilizes at $1.50 \times 10^{-4} \text{ cm s}^{-1}$ after 30 s hydrogenation. Such a trend is reproducible for different batches (Supplementary Figure 5a, b and Supplementary Note 4).

The total electrical capacitance (C_{tot}) per unit area of graphene, consists of the electrical double layer capacitance (C_{dl}) and the graphene quantum capacitance (C_{q}) connected in series³⁶. C_{tot} can be obtained either by using a lock-in technique (Methods) or by measuring the capacitive CV current for different scan rates, which is an averaged evaluation over a relatively wide potential ($C_{\text{ave-tot}}$, Supplementary Figure 6 and Supplementary Note 5). Additionally, the basic rectangular shapes of the capacitive current curves imply a purely capacitive behavior without Faradaic processes. Furthermore, upon hydrogenation $C_{\text{ave-tot}}$ first increases after 1 s, then drops till 10 s and saturates till 30 s, varying similarly as k^0 (Fig. 3d). The observed changes in $C_{\text{ave-tot}}$ can be mainly attributed to the DOS variations with hydrogenation (as C_{q} dominates in the series circuit).

Electrochemistry of H- sp^3 vs vacancy defects. To further evaluate the exact impact of defects on the electrochemical kinetics of graphene, we also studied samples that were treated with an argon plasma (referred as Ar-graphene) with comparable defect densities as to hydrogenated graphene (Supplementary Figure 7 and Supplementary Note 6). In contrast to the sensitive electrochemical behavior in H-graphene (Fig. 3a, c), both the current density and k^0 on Ar-graphene show negligible sensitivity to the argon plasma treatment (Fig. 3e, f). Such trends are consistent with the previous report that a low density of vacancy defects hardly impacts the electrochemical activity of graphene²⁶.

Based on the different $I(D)/I(D')$ ratios characterized using Raman spectroscopy (i.e., ~ 7 for Ar-graphene and ~ 10 for H-graphene)³⁷, we identify that argon plasma forms vacancy defects

by removing carbon atoms, while hydrogenation changes graphene hybridization from sp^2 to sp^3 . Thus, we gain insight into the driving mechanism for the observed electrochemical behavior. Rather than the vacancy defect, the change of hybridization (in H-graphene) is closely related to the electrochemical properties of hydrogenated graphene (Fig. 3). Meanwhile, coincident to the boost of k^0 , the G_{min} and μ increase slightly after 1 s of hydrogenation (Fig. 2), indicating a cleaner graphene with less surface scattering centers: hydrogen radicals are expected to react with the hydrocarbons adsorbed on the surface of graphene. Such a cleaning effect is due to the much higher reactivity of hydrocarbons with hydrogen radicals compared to the reactivity of the graphene itself with the same radicals. As airborne contaminations, hydrocarbons can adsorb onto any surface, as revealed from the observation that the wetting of graphitic surface dramatically changes over short time periods³⁸. Indeed, such cleaning effect is in agreement with prior observations that graphite—more specifically freshly exfoliated highly oriented pyrolytic graphite—exhibits high but instantly decaying electrochemical activity due to the exposure to airborne contaminants^{39,40}. Notably, we expect no cleaning effect using argon plasma under our condition (ion energy $\sim 60 \text{ eV}$)⁴¹, as also confirmed by the high-resolution transmission electron microscopy images of Ar-graphene (not shown here).

In addition, we employed X-ray photoelectron spectroscopy (XPS, Supplementary Figure 8 and Supplementary Note 7) in complementary to Raman to compare graphene containing similar defect densities (according to Raman analysis) after 60 s of hydrogenation and after 15 s of argon plasma treatment. The presence of C- sp^2 (284 eV), C- sp^3 (285 eV), C-O (286–286.2 eV), and C=O (287.8–288 eV) in C 1s spectra, suggest that both samples contain sp^2 and sp^3 carbon with minor oxygen contaminants from PMMA residues (only used for XPS samples to transfer graphene onto the Si substrate). As XPS probes both the surface chemistry of graphene and its surface adsorbents, we observed a higher content of sp^3 carbon from XPS analysis (Supplementary Table 1), compared to the results of Raman spectroscopy. Thus, we ascribe the observed sp^3 C in both H-graphene (6.2–8.0%) and Ar-graphene (3%) to possible surface adsorbents including PMMA residues and

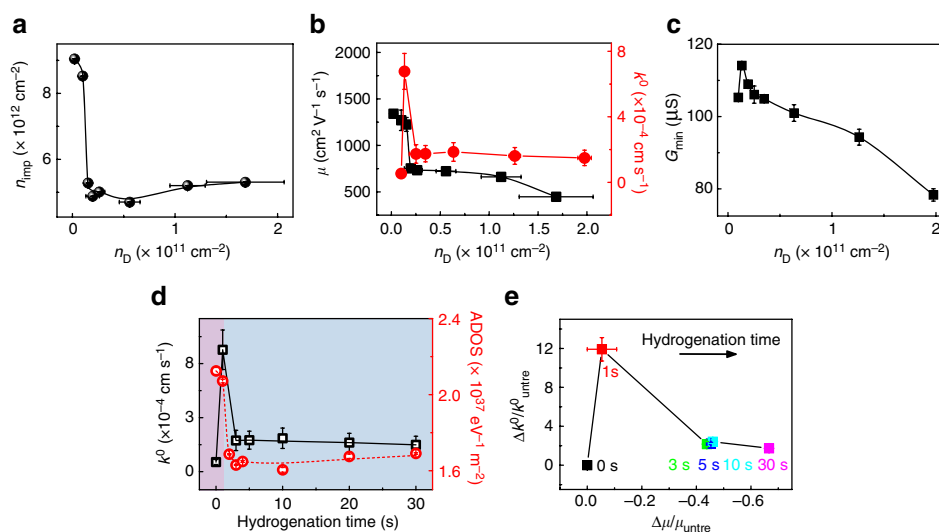


Fig. 4 Quantum and electrochemical interplays in hydrogenated graphene. **a** The dependence of n_{imp} on n_{D} . **b** Correlations of μ and k^0 with n_{D} , respectively. **c** The minimum conductivity (G_{min}) vs n_{D} . **d** The correspondence between ADOS and k^0 as a function of the hydrogenation time. The purple region represents the cleaning-dominated regime and the blue region represents the regime where the chemical modification dominates. **e** The relative variations of $\Delta\mu/\mu_{\text{untre}}$ correlating with $\Delta k^0/k^0_{\text{untre}}$ according to the corresponding hydrogenation time. The subscript "untre" represents the untreated graphene. The error bars are the standard deviation of experimental values

hydrocarbons. A trace amount of sp^3 doping in the graphene lattice (up to 0.8% sp^3 C in H-graphene) was, however, determined by Raman spectroscopy.

Correlation of n_D with n_{imp} . To shed light on the influence of the electrochemical current on the performance of GFET sensors, we discuss here the interplay between the in-plane charge transport and the electrochemical activity of H-graphene. Particularly, we systematically investigate the correlations between the DOS, the mobility of charge carriers μ , and the electron transfer rate k^0 , with respect to the density of charged impurity n_{imp} and defect density n_D . Finally, we provide a comprehensive discussion on the driving mechanism for the electrical and electrochemical behavior we observe for H-graphene.

To understand the correlation between defect density n_D and impurity density n_{imp} (presented in Fig. 4a), it is important to consider their relation to the electronic properties of graphene. It is well-known from studies on supported graphene that defects yield short-range electron scattering in graphene. Impurities, on the other hand, cause long-range (Coulomb) scattering resulting in trapped electron states. The overall conductivity of graphene is dictated by the prevalence of either impurities or defects in the sample; n_D dominates at high charge carrier density while n_{imp} determines at low charge carrier density^{28,42}. Impurities are generally present at the interfaces between graphene and air or between graphene and the underlying substrate. The cleaning effect in the first second of hydrogenation appears in Fig. 4a as the decreasing onset for n_{imp} (from 9.05 to $8.52 \times 10^{12} \text{ cm}^{-2}$).

Aside from the cleaning effect, the subsequent dramatic drop in n_{imp} from $8.52 \times 10^{12} \text{ cm}^{-2}$ to $5.01 \times 10^{12} \text{ cm}^{-2}$ (2–5 s) can be ascribed to the hybridization change from sp^2 to sp^3 when n_D steadily increases with hydrogenation. The presence of sp^3 hybridized spots in the lattice causes the lattice to expand and to curve. The increased distance between the lattice and substrate-related impurities explains the sharp drop in n_{imp} . Further on, n_{imp} slightly increases (from $5.01 \times 10^{12} \text{ cm}^{-2}$ to $5.31 \times 10^{12} \text{ cm}^{-2}$), which can be ascribed to the accumulation of trapped water molecules at the graphene surface, accompanying the increasing n_D ($n_D > (2.6 \pm 0.5) \times 10^{10} \text{ cm}^{-2}$).

Correlation of k^0 and μ with n_D . The first report on the correlation of k^0 with the density of vacancy defects in monolayer graphene showed that k^0 remained constant at low densities but underwent a tenfold increase at a defect density of 10^{12} cm^{-2} ($I(D)/I(G) \cong 2.95$)²⁶. However, the high density of vacancy defects lowers the electrical performance of graphene. In our work, k^0 is improved up to 12-fold (to $6.77 \times 10^{-4} \text{ cm s}^{-1}$) at a low H- sp^3 defect density of $n_D = (1.0 \pm 0.1) \times 10^{10} \text{ cm}^{-2}$ ($I(D)/I(G) \cong 0.4$). Then, when n_D continues to rise, k^0 drops sharply to stabilize between 1.5 and $1.7 \times 10^{-4} \text{ cm s}^{-1}$ (red line, Fig. 4b).

Separately, when k^0 increases, the carrier mobility μ stays unchanged (or becomes slightly higher) compared to untreated graphene (black line, Fig. 4b) at $n_D = (1.0 \pm 0.1) \times 10^{10} \text{ cm}^{-2}$. With the continuous growth of the defect density up to $n_D = (2.0 \pm 0.7) \times 10^{10} \text{ cm}^{-2}$, μ exhibits a deep drop, indicating that the carrier transport in graphene is sensitive to the existence of even low densities of H- sp^3 defects ($n_D \leq (2.0 \pm 0.7) \times 10^{10} \text{ cm}^{-2}$ corresponding to a distance L_D of ~ 40 nm between the defects). For higher defect densities, however, the decrease of μ is less pronounced (till $n_D = (1.7 \pm 0.4) \times 10^{11} \text{ cm}^{-2}$, that is $L_D \sim 14$ nm). The minimum conductivity (G_{min}) changes with n_D in Fig. 4c, correlating well with the fluctuations in mobility (Fig. 4b).

Based on the Boltzmann theory, the conductivity of graphene (G) is proportional to $1/(n_D)^{1/2}$ at high carrier density (far from the CNP)⁴³. In consequence, μ is expected to decrease with

increasing n_D upon hydrogenation. Meanwhile, at low carrier density (near the CNP), G is proportional to $(n_{imp})^{1/2}$ and G_{min} is expected to reduce with the decrease of n_{imp} . The data in Fig. 4b, c fit the theory, except for the increase in both G_{min} and μ upon the initial hydrogenation ($n_D = (1.0 \pm 0.1) \times 10^{10} \text{ cm}^{-2}$). This can be explained by considering the cleaning of adsorbates from the graphene surface. Particularly, hydrogenation slightly introduces H- sp^3 defect while also removing surface short-range scatters outweighing the effect on the conductivity and mobility of graphene. Separately, the decrease of the DOS after hydrogenation contributes to the decrease of the density of intrinsic charge carrier n instead of affecting the carrier mobility of these charge carriers in graphene.

Correlation between the DOS and k^0 . In electrochemistry, the kinetics of electron transfer from graphene to a redox probe is dependent on the electrochemical potential of electrons in graphene (that is the Fermi level, E_F) with respect to the electrochemical potential of the redox couple in solution^{31,44}. For example, for the electron to flow from the redox probe to graphene, the graphene E_F that can be tuned by varying the potential applied to the graphene electrode or by sweeping the gate voltage, should at least align with the LUMO level of the oxidative molecule to allow an efficient electron transfer. For a non-adiabatic process, the DOS in graphene decides—whether or not—a basal plane electron could tunnel to the redox probe. Practically, the electron transfer occurs when the electronic resonance between the redox molecule and graphene is reached, that is for a given value of the applied potential, and is measured by studying how fast the electron transfer reaction can reach its equilibrium (kinetics)⁴⁵. In short, the electrochemical kinetics (reflected by k^0) of graphene relies on the DOS on the premise of non-adiabatic electron transfer.

In 2D materials like graphene, its minimal quantum capacitance, $C_{q,min}$, can be used to deduce its average DOS (ADOS) at a specific E_F : $\rho = C_{q,min}/e^2$, where e is the electron charge⁴⁶. In Fig. 4d, we therefore plot and compare the ADOS with k^0 as hydrogenation proceeds. During the first second (within the purple region), the ADOS decreases a little, however k^0 increases dramatically, which can be mainly ascribed to the volatilization of hydrocarbon contaminants. That is, the hydrogen radicals first remove the hydrocarbon adsorbates to reveal the electrochemical activity of the underlying graphene, as the kinetic process involves interface-sensitive electron tunneling. Notably, H radicals can also attack the graphene lattice during the hydrocarbon cleaning and the resulting H- sp^3 defect could lead to the observed decrease in the ADOS²⁶. Upon further hydrogenation (the beginning of the blue region), the ADOS and k^0 decrease sharply, which are mainly due to the modification of the graphene basal plane by hydrogen radicals. The decay of k^0 with DOS agrees with the non-adiabatic electron transfer, in which the rate depends on the electronic properties of the electrode due to the weak electronic interaction between the redox mediator and the electrode, according to the Levich–Dogonadze theory⁴⁷ and Fermi's golden rule⁴⁸. We would like to note here that the decrease in k^0 (Fig. 4d) is unlikely due to H- sp^3 termination, as the formed C–H dipole is more susceptible towards nucleophilic attack⁴⁹, which could increase the electrochemical activity. Nor is it likely that the kinetics were affected by surface oxidation during exposure to air: XPS spectra demonstrate the negligible oxidation of H-graphene after its exposure to the ambient conditions even for 1 week (Supplementary Figure 8 and Supplementary Table 1). Additionally, the DOS was predicted to contribute more significantly to the kinetics compared to surface modification⁴⁰. Thus we demonstrate for the first time, that the electrochemical kinetics

in the single layer graphene is highly sensitive to the ADOS upon the addition of even a single H- sp^3 defect per 100,000 sp^2 carbon atoms. More importantly, the correlation between k^0 and DOS in return confirms the importance of graphene electronic properties (DOS) in terms of defining the electrochemical current for sensing application.

Correlation between μ and k^0 . Figure 4e shows the dependence of the relative variation of $\Delta k^0/k_{\text{untre}}^0$ with $\Delta\mu/\mu_{\text{untre}}$, where $\Delta k^0/k_{\text{untre}}^0 = \frac{k^0 - k_{\text{untre}}^0}{k_{\text{untre}}^0}$, $\Delta\mu/\mu_{\text{untre}} = \frac{\mu - \mu_{\text{untre}}}{\mu_{\text{untre}}}$, and the subscript “untre” denotes untreated graphene. Notably, the negative values of $\Delta\mu/\mu_{\text{untre}}$ corresponds to the degradation of the carrier mobility upon hydrogenation time (see also Fig. 2). Specifically, the peak value of the $\Delta k^0/k_{\text{untre}}^0$ after 1 s of hydrogenation is ascribed to the disclosure of the intrinsic electrochemical activity of the graphene basal plane resulting from the volatilization of hydrocarbon adsorbates. For hydrogenation times longer than 3–5 s, $\Delta k^0/k_{\text{untre}}^0$ decreases by ~ 5 times compared to the peak value (at 1 s) with preserved mobility (~ 50 – 60%). Our results therefore suggest the importance of H- sp^3 defects towards achieving a low electrochemical activity in GFET by suppressing its DOS. Interestingly, the boosted k^0 upon H₂ plasma cleaning reveals a relatively high electrochemical activity of the graphene basal plane, which was often believed to be inert and inactive in electrochemistry⁵⁰.

Discussion

We demonstrated that a hydrogen radical plasma cleans the surface of graphene and chemically modifies the graphene lattice upon continuous exposure. In the beginning (the first 1–5 s), the introduced H radicals mainly sweep the hydrocarbon adsorbates away from the graphene surface. In particular, within the first second of hydrogenation we observed a large enhancement of the electrochemical activity on the surface of pristine graphene (with a minimum of H- sp^3 defects). We postulate that in untreated graphene, the electrochemical activity was initially blocked by the presence of hydrocarbon adsorbates which are now removed by the hydrogen plasma⁵¹ (Fig. 3c and Fig. 4d). Remarkably, even traces amounts of H- sp^3 defects in graphene (only one sp^3 defect per $\sim 400,000$ carbon atoms) results in the decrease of the DOS, a quantity considerably sensitive to the changes of electronic and chemical properties of graphene. Additionally, further hydrogenation of the graphene basal plane largely depresses k^0 down to one fifth of its original value (pristine graphene), presumably by lowering its DOS. Interestingly, however, the mobility of graphene is preserved to a large extent (Fig. 2), promising future development of electrochemical field-effect transistors based on H-graphene.

Besides hydrogenation, the physisorption of water molecules at the graphene surface reflected by the observed p-doping effect (Fig. 2b)²⁵ is also considered. As non-covalent functionalization, water molecules can barely disturb the intrinsic aromaticity⁵², thus we expect that it exerts little impact on the electronic structure and electrochemistry of graphene⁵³. For example, the resistivity at the CNP as well as the carrier mobility barely changed after removal of the adsorbed water²⁵. Separately, negligible oxidation is found using XPS characterization even in aged graphene, as shown in Supplementary Figure 5. Therefore we can exclude the major contributions of surface-adsorbed water and graphene oxidation to the observed electrical and electrochemical properties of hydrogenated graphene.

In summary, we have systematically probed the interplay between the in-plane electron transport and the electrochemical activity of the graphene basal plane by modulating the density of H- sp^3 defects. Interestingly, the mild hydrogenation within 1–5 s

largely preserves the basic electrical mobility while effectively depresses the electrochemical kinetics k^0 and lowers the DOS in graphene, manifesting as a plausible way to improve the sensitivity of GFET. For the first time, we demonstrated that the electrochemical kinetics in single layer H-graphene is highly dependent on the ADOS, which supports the theory of non-adiabatic electron transfer on graphene. Additionally, the electrochemical activity of the pristine graphene basal plane can be restored by the removal of surface-adsorbed hydrocarbons using a low dose of hydrogen radicals, a result that will further promote graphene as an electrode for electrochemical studies. The correlation between the carrier mobility and the electrochemical kinetics suggests that the electrical conductivity of H-graphene is an important parameter to consider, for example, in GEC sensors. We believe our work will inspire several research communities to consider hydrogenated graphene as a potent material for sensing applications with performances going beyond previously reported (G)FET sensors.

GFET device fabrication. To fabricate the GFET devices, the graphene side of the copper growth substrate (CVD graphene, Graphenea S.A.) is glued to a glass slide with a PETMP-TATATO polymer²³. PETMP-TATATO (Sigma Aldrich) is a clean and biocompatible polymer usually used for dental restorative application²⁴. After sufficient photo-initiated cross-linking reaction at room temperature (12 h in daylight), the whole stack (glass-glue-graphene-copper) was oxidized with an O₂ plasma (60 W/0.5 mbar/2 min) to remove the trace of graphene that had grown on the backside of the copper substrate (i.e. the side now facing to the air). To fabricate the source and drain electrodes, both ends of the copper substrate (a strip of copper) were protected by a polymer film of cellulose acetate butyrate (CAB, 30 mg mL⁻¹ in ethyl acetate, Sigma Aldrich). Then an ammonium persulfate solution (0.5 M) was used to etch the non-protected copper foil to reveal the clean CVD graphene supported by the photopolymer and glass substrate without any possible polymer residues. Finally, the fabricated graphene devices were exposed to a hydrogen plasma for different durations to introduce defects with controlled densities.

Thiol-enes polymer. Commercially available pentaerythritol tetra(3-mercaptopropionate) and triallyl-1,3,5-triazine-2,4,6-trione (referred to as PETMP and TATATO, respectively) are used as monomers for the thiol-ene resin formulation. 4:3 volume proportion of PETMP-TATATO were selected for the preparation of the photopolymer.

Plasma condition. Capacitively coupled plasma system with the radio-frequency (RF) of 40 kHz and 200 W power from Diener electronic (Femto) was employed at room temperature. The base pressure of this system is <0.02 mbar. The parameters used for the controlled introduction of defects were 10 W/1.0 mbar for hydrogen plasma and 8 W/0.85 mbar for argon plasma. Specifically, a Faraday cage with grid was employed to shield all the energetic hydrogen ions to form a mild radical plasma to react with graphene.

Characterization. Raman spectroscopy and mapping were collected from both exfoliated graphene and CVD graphene (using the PMMA transfer method⁵⁴) on Si/SiO₂ substrate. Raman spectra of CVD graphene on PETMP-TATATO polymer was also performed (Supplementary Figure 2a). The Raman spectrometer used is a WITTEC alpha300 R-Confocal Raman Imaging with a laser wavelength of 532 nm. To minimize the potential damage from laser heating effect, the laser power was controlled under

1.1 mW. All of the measurements were performed under ambient conditions at room temperature. XPS data were collected from a K-Alpha X-ray photoelectron spectrometer by Thermo Scientific. SEM images were carried out on a JEOL SEM 6400 microscope. A JPK NanoWizard Ultra Speed AFM was employed to characterize the topology of exfoliated graphene before and after hydrogenation on a Si/SiO₂ substrate. The images were scanned in an intermittent contact mode in air at room temperature.

Electrical measurement. The transport measurements of GFET devices upon different hydrogenation times were performed on a SR830 DSP lock-in amplifier with narrow filters. Electrolyte- or electrochemical-gated GFET measurements were carried out in 0.1 M KCl solution containing 10 mM Tris as the buffer (pH 8, both from Sigma Aldrich). The gate voltage was applied on a AgCl/Ag wire as the reference electrode, at a sweep rate at 100 mV s⁻¹, while the source/drain current was fixed at 0.1 μA.

Quantum capacitance. As illustrated in Supplementary Figure 4, the total capacitance C_{tot} of an electrolyte-gated GFET, is composed of two components in series, quantum capacitance C_q and the electric double-layer capacitance C_{dl} . The C_{dl} for the KCl solution can be approximated as 10–20 μF cm⁻² for a wide range of ionic concentration >1 mM⁵⁵. C_q is relatively small (~1 μF cm⁻²) compared to the C_{dl} (in series) and thus dominates the total capacitance $C_q \sim C_{\text{tot}}$ ³². By calculating the C_q based on $1/C_{\text{tot}} = 1/C_q + 1/C_{\text{dl}}$, we get the curves of C_q vs the potential distributed on graphene channel V_{ch} ($V_{\text{ch}} = (V_g C_{\text{dl}})/(C_{\text{dl}} + C_q)$) for different hydrogenation times.

Electrochemical measurement. The electrochemical experiments were carried out in a homemade one-compartment three-electrode electrochemical cell at ambient conditions. The working electrode is the CVD grown graphene and the counter electrode a platinum wire. All potentials in this work are reported with respect to a saturated Ag/AgCl reference electrode. A potentiostat/galvanostat (CompactStat, Ivium Technologies) was used for the electrochemical measurements. The electrolyte, 0.1 M KCl, was prepared from KCl (Sigma Aldrich, ≥98%) and ultrapure water (Millipore Milli-Q gradient A10 system, 18.2 MΩ cm). The measured current was normalized to the geometric surface area of the working electrode and not corrected for Ohmic drop as the obtained currents were very low. Prior to the experiments, the cell containing the electrolyte solution was purged with argon to remove the dissolved oxygen.

Data availability. The data that support the findings of this study are available from the corresponding author on request.

Received: 4 April 2017 Accepted: 15 January 2018

Published online: 23 February 2018

References

- Zhang, A. & Lieber, C. M. Nano-bioelectronics. *Chem. Rev.* **116**, 215–257 (2015).
- Fu, W., Jiang, L., van Geest, E. P., Lima, L. & Schneider, G. F. Sensing at the surface of graphene field-effect transistors. *Adv. Mater.* **29**, 1603610 (2017).
- Hwang, M. T. et al. Highly specific SNP detection using 2D graphene electronics and DNA strand displacement. *Proc. Natl Acad. Sci. USA* **113**, 7088–7093 (2016).
- Gao, N. et al. Specific detection of biomolecules in physiological solutions using graphene transistor biosensors. *Proc. Natl Acad. Sci. USA* **113**, 14633–14638 (2016).
- Wang, Y., Shao, Y., Matson, D. W., Li, J. & Lin, Y. Nitrogen-doped graphene and its application in electrochemical biosensing. *ACS Nano* **4**, 1790–1798 (2010).
- Xia, Z. et al. Electrochemical functionalization of graphene at the nanoscale with self-assembling diazonium salts. *ACS Nano* **10**, 7125–7134 (2016).
- Fortgang, P. et al. Robust electrografting on self-organized 3D graphene electrodes. *ACS Appl. Mater. Interfaces* **8**, 1424–1433 (2016).
- Eng, A. Y. S. et al. Hydrogenated graphenes by Birch reduction: influence of electron and proton sources on hydrogenation efficiency, magnetism, and electrochemistry. *Chem. Eur. J.* **21**, 16828–16838 (2015).
- Eigler, S. & Hirsch, A. Chemistry with graphene and graphene oxide—challenges for synthetic chemists. *Angew. Chem. Int. Ed.* **53**, 7720–7738 (2014).
- Bai, Z., Zhang, L. & Liu, L. Bombarding graphene with oxygen ions: combining effects of incident angle and ion energy to control defect generation. *J. Phys. Chem. C* **119**, 26793–26802 (2015).
- Bagri, A. et al. Structural evolution during the reduction of chemically derived graphene oxide. *Nat. Chem.* **2**, 581–587 (2010).
- Sun, Z. et al. Towards hybrid superlattices in graphene. *Nat. Commun.* **2**, 559 (2011).
- Elias, D. C. et al. Control of graphene's properties by reversible hydrogenation: evidence for graphane. *Science* **323**, 610–613 (2009).
- Nair, R. R. et al. Fluorographene: a two-dimensional counterpart of Teflon. *Small* **6**, 2877–2884 (2010).
- Son, J. et al. Hydrogenated monolayer graphene with reversible and tunable wide band gap and its field-effect transistor. *Nat. Commun.* **7**, 13261 (2016).
- Tuinstra, F. & Koenig, J. L. Raman spectrum of graphite. *J. Chem. Phys.* **53**, 1126–1130 (1970).
- Lespade, P., Marchand, A., Couzi, M. & Cruege, F. Characterisation de matériaux carbonés par microspectrométrie Raman. *Carbon* **22**, 375–385 (1984).
- Eckmann, A. et al. Probing the nature of defects in graphene by Raman spectroscopy. *Nano Lett.* **12**, 3925–3930 (2012).
- Das, A. et al. Monitoring dopants by Raman scattering in an electrochemically top-gated graphene transistor. *Nat. Nanotechnol.* **3**, 210–215 (2008).
- Wang, Q. H., Shih, C.-J., Paulus, G. L. & Strano, M. S. Evolution of physical and electronic structures of bilayer graphene upon chemical functionalization. *J. Am. Chem. Soc.* **135**, 18866–18875 (2013).
- Cançado, L. G. et al. Quantifying defects in graphene via Raman spectroscopy at different excitation energies. *Nano Lett.* **11**, 3190–3196 (2011).
- Ferrari, A. C. & Basko, D. M. Raman spectroscopy as a versatile tool for studying the properties of graphene. *Nat. Nanotechnol.* **8**, 235–246 (2013).
- Fu, W. et al. High mobility graphene ion-sensitive field-effect transistors by noncovalent functionalization. *Nanoscale* **5**, 12104–12110 (2013).
- Cramer, N. B. et al. Investigation of thiol-ene and thiol-ene-methacrylate based resins as dental restorative materials. *Dent. Mater.* **26**, 21–28 (2010).
- Matis, B. R. et al. Surface doping and band gap tunability in hydrogenated graphene. *ACS Nano* **6**, 17–22 (2012).
- Zhong, J.-H. et al. Quantitative correlation between defect density and heterogeneous electron transfer rate of single layer graphene. *J. Am. Chem. Soc.* **136**, 16609–16617 (2014).
- Schedin, F. et al. Detection of individual gas molecules adsorbed on graphene. *Nat. Mater.* **6**, 652–655 (2007).
- Hwang, E., Adam, S. & Sarma, S. D. Carrier transport in two-dimensional graphene layers. *Phys. Rev. Lett.* **98**, 186806 (2007).
- Trushin, M. & Schliemann, J. Conductivity of graphene: how to distinguish between samples with short- and long-range scatterers. *Eur. Lett.* **83**, 17001 (2008).
- Balakrishnan, J., Koon, G. K. W., Jaiswal, M., Neto, A. C. & Özyilmaz, B. Colossal enhancement of spin-orbit coupling in weakly hydrogenated graphene. *Nat. Phys.* **9**, 284–287 (2013).
- Heller, I., Kong, J., Williams, K. A., Dekker, C. & Lemay, S. G. Electrochemistry at single-walled carbon nanotubes: the role of band structure and quantum capacitance. *J. Am. Chem. Soc.* **128**, 7353–7359 (2006).
- Xia, J., Chen, F., Li, J. & Tao, N. Measurement of the quantum capacitance of graphene. *Nat. Nanotechnol.* **4**, 505–509 (2009).
- Adam, S., Hwang, E., Galitski, V. & Sarma, S. D. A self-consistent theory for graphene transport. *Proc. Natl Acad. Sci. USA* **104**, 18392–18397 (2007).
- Velicky, M. et al. Electron transfer kinetics on mono- and multilayer graphene. *ACS Nano* **8**, 10089–10100 (2014).
- Nicholson, R. S. Theory and application of cyclic voltammetry for measurement of electrode reaction kinetics. *Anal. Chem.* **37**, 1351–1355 (1965).
- Ji, H. et al. Capacitance of carbon-based electrical double-layer capacitors. *Nat. Commun.* **5**, 3317 (2014).
- Eckmann, A., Felten, A., Verzhbitskiy, I., Davey, R. & Casiraghi, C. Raman study on defective graphene: effect of the excitation energy, type, and amount of defects. *Phys. Rev. B* **88**, 035426 (2013).
- Li, Z. et al. Effect of airborne contaminants on the wettability of supported graphene and graphite. *Nat. Mater.* **12**, 925–931 (2013).
- Patel, A. N. et al. A new view of electrochemistry at highly oriented pyrolytic graphite. *J. Am. Chem. Soc.* **134**, 20117–20130 (2012).

40. Velický, M. et al. Electron transfer kinetics on natural crystals of MoS₂ and graphite. *Phys. Chem. Chem. Phys.* **17**, 17844–17853 (2015).
41. Lim, Y.-D. et al. Si-compatible cleaning process for graphene using low-density inductively coupled plasma. *ACS Nano* **6**, 4410–4417 (2012).
42. Chen, J.-H. et al. Charged-impurity scattering in graphene. *Nat. Phys.* **4**, 377–381 (2008).
43. Adam, S., Hwang, E., Rossi, E. & Sarma, S. D. Theory of charged impurity scattering in two-dimensional graphene. *Solid State Commun.* **149**, 1072–1079 (2009).
44. Paulus, G. L., Wang, Q. H. & Strano, M. S. Covalent electron transfer chemistry of graphene with diazonium salts. *Acc. Chem. Res.* **46**, 160–170 (2012).
45. Adams, D. M. et al. Charge transfer on the nanoscale: current status. *J. Phys. Chem. B* **107**, 6668–6697 (2003).
46. Eisenstein, J., Pfeiffer, L. & West, K. Negative compressibility of interacting two-dimensional electron and quasiparticle gases. *Phys. Rev. Lett.* **68**, 674 (1992).
47. Levich, V. *Physical Chemistry, and Advanced Treatise* (Academic, New York, 1970).
48. Nissim, R., Batchelor-McAuley, C., Henstridge, M. C. & Compton, R. G. Electrode kinetics at carbon electrodes and the density of electronic states. *Chem. Commun.* **48**, 3294–3296 (2012).
49. Debela, A. M., Ortiz, M., Beni, V. & O'Sullivan, C. K. Facile electrochemical hydrogenation and chlorination of glassy carbon to produce highly reactive and uniform surfaces for stable anchoring of thiolated molecules. *Chem. Eur. J.* **20**, 7646–7654 (2014).
50. Brownson, D. A., Kampouris, D. K. & Banks, C. E. Graphene electrochemistry: fundamental concepts through to prominent applications. *Chem. Soc. Rev.* **41**, 6944–6976 (2012).
51. Li, Z. et al. Water protects graphitic surface from airborne hydrocarbon contamination. *ACS Nano* **10**, 349–359 (2015).
52. Zhang, Z., Huang, H., Yang, X. & Zang, L. Tailoring electronic properties of graphene by π - π stacking with aromatic molecules. *J. Phys. Chem. Lett.* **2**, 2897–2905 (2011).
53. Peng, Y., Wang, J., Lu, Z. & Han, X. Adsorption of the water molecule on monolayer graphene surface has effect on its optical properties. *IOP Conf. Ser.: Mater. Sci. Eng.* **87**, 012101 (2015).
54. Liang, X. et al. Toward clean and crackless transfer of graphene. *ACS Nano* **5**, 9144–9153 (2011).
55. Baldelli, S. Surface structure at the ionic liquid-electrified metal interface. *Acc. Chem. Res.* **41**, 421–431 (2008).

Acknowledgements

The research leading to this work has gratefully received funding from the Chinese Scholarship Council (L.J., 201406890016), the European Research Council under the

European Union's Seventh Framework Programme (FP/2007-2013)/ERC Grant Agreement no. 335879 project acronym "Biographene", the Netherlands Organization for Scientific Research (Vidi 723.013.007 and Veni 722.014.004), and the Swiss National Science Foundation (P300P2_154557). L.J. appreciates Prof. Dr. Ute Kaiser, Dr. Haoyuan Qi, and Liubov Belyaeva for helpful discussions. L.J. appreciates Pauline van Deursen for proofreading the manuscript.

Author contributions

L.J., W.F. and G.F.S. designed the experiments. G.F.S. supervised and coordinated the research. L.J. performed all the sample preparations, characterizations, and measurements with the support of W.F. L.J. and W.F. analyzed the data and constructed the discussion. Y.Y.B. and M.T.M.K. provided the electrochemical working station, and contributed to the electrochemical experiments and analysis. L.J., W.F., and G.F.S. wrote the manuscript. All authors read and commented the manuscript. L.J. and W.F. contributed equally.

Additional information

Supplementary Information accompanies this paper at <https://doi.org/10.1038/s41467-018-03026-0>.

Competing interests: The authors declare no competing financial interests.

Reprints and permission information is available online at <http://npg.nature.com/reprintsandpermissions/>

Publisher's note: Springer Nature remains neutral with regard to jurisdictional claims in published maps and institutional affiliations.



Open Access This article is licensed under a Creative Commons Attribution 4.0 International License, which permits use, sharing, adaptation, distribution and reproduction in any medium or format, as long as you give appropriate credit to the original author(s) and the source, provide a link to the Creative Commons license, and indicate if changes were made. The images or other third party material in this article are included in the article's Creative Commons license, unless indicated otherwise in a credit line to the material. If material is not included in the article's Creative Commons license and your intended use is not permitted by statutory regulation or exceeds the permitted use, you will need to obtain permission directly from the copyright holder. To view a copy of this license, visit <http://creativecommons.org/licenses/by/4.0/>.

© The Author(s) 2018